On the Possibilities of Using a Brushless Doubly-Fed Reluctance Generator in a 2 MW Wind Turbine

David G Dorrell
Dept of Electronics and Electrical Engineering
University of Glasgow
Glasgow, G12 8LT, UK

Milutin Jovanovic
School of Computing, Engineering & Information Sciences
Northumbria University
Newcastle upon Tyne, NE1 8ST, UK

***Abstract*— The paper will put a forward a description of a realistic design for a brushless doubly-fed machine that is of practical value. It takes the form a 4-pole / 8-pole machine aimed for use in a 2 MW wind turbine over a correct speed and torque range. Previous examples discussed laboratory machines and this study takes the outcomes from these studies to formulate a procedure for sizing and designing the machine. The latest design and analysis techniques are used, with practical rotor ducting considered. Control is also addressed in the paper, in particular the assessment of sensorless reactive power control. This paper is aimed at taking the machine from a small-scale laboratory example to consideration as a large-size industrial generation and therefore it represents a step-change in the literature on the machine.**

Keywords- Doubly-fed reluctance generator, wind turbines

I. INTRODUCTION

Wind turbines use either a cage-rotor induction generator, a variable speed synchronous generator or, more recently, a doubly-fed wound-field induction generator (with the field fed from a converter and main windings fed connected to the grid - DFIG). These are usually connected to the turbine via a gearbox although large-diameter direct-drive generators do exist. The wound-field induction generator is now very common but it has reliability issues due to the slip rings. This may be an obstacle for its wider use, for example, in off-shore wind turbines where operation and maintenance costs can be significant [12]. Researchers are now investigating brushless doubly-fed generators where there are two sets of 3-phase windings – these will have different pole numbers (say 2 and 6 poles, as often used in the literature, or a 4 and 8 pole combination as used here) with one connected to the grid (power winding) and one controlled via a converter (control winding). There are two alternatives for this machine: induction type (with the rotor formed from bars connected in nested loops) and the brushless doubly-fed reluctance machine type (with a salient pole rotor similar to switched reluctance machine or an axially-laminated rotor) – the BDFRM. The BDFRM rotor does not have a cage or windings. This 'cold' rotor is more mechanically robust and allows simple modeling and control as well as higher efficiency [13].

This paper reports on a study of the electromagnetic analysis of the doubly-fed radially-laminated reluctance generator. A recent paper [1] assessed the iron losses generated in the axially-laminated machine and debated whether the correct option should be to use a radially-laminated rotor to reduce the rotor losses. This was expanded upon in [2]. The control of these machines has already been studies extensively [3]-[7]. While work on the electromagnetic design was carried out in [8]. The correct design of this type of machine is still under investigation; [9] studied the conversion of an induction machine with a specially constructed rotor. It was found that it was difficult to get the correct electrical loading because there was insufficient slot space.

Another recent paper [10] developed an algorithm for the correct design of a machine using a salient-pole reluctance machine. The design focused on the radially-laminated nominally 7.5 kW machine. Initially the design took the axially-laminated machine in [1] and redesigned the rotor with a radially-laminated rotor. The procedure took the stator and redesigned the lamination to give the correct slot area. This was done by essentially increasing the slot depth and outer diameter. This paper highlighted various issues with this design on machine. Firstly that the 2/6 pole combination is quite a poor combination. This is because cross coupling occurs between the stator winding sets not only through the rotor permeance modulation, but also through 3rd harmonic saturation of 2-pole winding. Secondly, while the axially-laminated rotor in [1] produces eddy current loss it is very pole-specific whereas the salient pole rotor is not as generalized and can produce modulations with further permeance harmonics. Fig. 1 shows these different rotor combinations. The third major design issue that was raised was the slot size. Previous prototypes have all been converted from induction machine designs with specially constructed rotors. However, this was found to be inappropriate because the rotor electrical loading, as present in a cage or DFIG wound rotor, is moved from the rotor to the stator. Therefore more stator slot area is needed – essentially the slot depth and stator outside diameter have to be increased to accommodate this.

Another alternative is to use a ducted rotor as shown in Fig. 2. This is similar to the axially-laminated rotor but there are much fewer ducts (8 per pole here) since radial laminations are used. This is a 6 pole rotor rather than the 4 pole rotors illustrated in Fig. 1. This is because a 2/6 pole was found to be poor so that a 4/8 pole combination was chosen here. It also shows increased slot area. The rotor has axial ducts (not necessarily air – they may be used for construction) and is radially laminated.

In this paper design for a 2 MW brushless reluctance generator will be developed to investigate its potential as a wind turbine generator. A full electromagnetic simulation will

978-1-4244-2279-1/08/$25.00 © 2008 IEEE

be conducted using finite element analysis. In the second part of the paper a control strategy is put forward which is necessary to control the machine. The results of the control simulations are described.

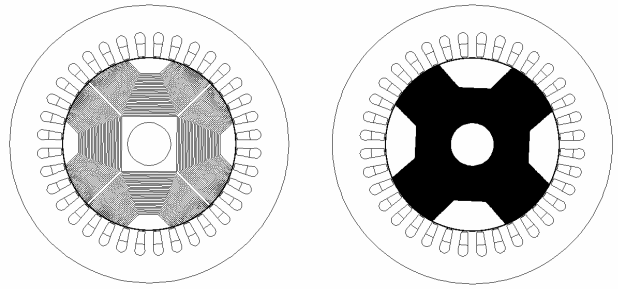

Fig. 1. Axially-laminated rotor and salient-pole radially-laminated reluctance rotor.

The control of the machine, in particular direct torque control (DTC) and sensorless control, is addressed below. To the best of the authors' knowledge, the only sensorless speed control algorithm for the BDFRM has been reported in [14], but without supporting test results to demonstrate its practical realization. A DTC scheme was proposed and simulated in [15], and experimentally verified in [16]. It was shown to overcome the usual deficiencies of the traditional DTC approaches and allowed stable machine operation down to zero applied frequency of the inverter-fed (secondary) winding (Fig. 2). However, while sensorless control of torque and flux was achieved in [15][16], the speed feedback information required for speed control was derived from rotor position measurements and not estimates.

The control section of this paper is complementary in nature to [15] and [16], and can be treated as a comprehensive extension to this previous theoretical work on sensorless DTC [17]. Unlike [17], where the maximum torque per inverter ampere property was considered, the conditions for maximum primary power factor control will be developed in the paper and it's successful practical implementation verified by experimental results. The latter will clearly show how a conventional load model based observer [18] can be effectively used for the machine speed identification from the estimated rotor position to achieve true encoderless speed control in real-time.

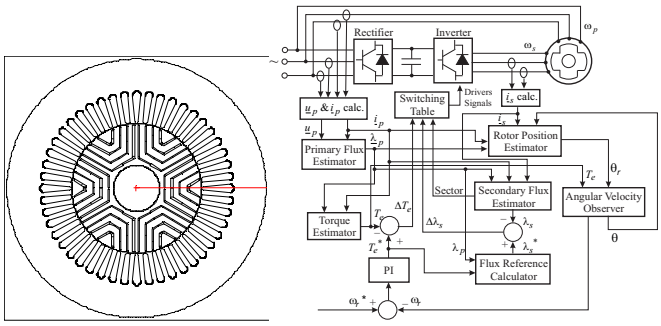

Fig. 2. Cross section of 4/8 pole machine with 6-pole ducted rotor and sensorless speed and direct torque (power) control of BDFRM.

II. MACHINE DESIGN CHOICES

A 2 MW turbine will usually rotate between about 10 rpm and 20 rpm with the peak power being reached at about 15 rpm. We need to set the speed range of the turbine. Taking the 8-pole winding to be the power winding, there is a synchronizing requirement for the non-grid connected control winding:

$$\omega_c = P\omega_r \pm \omega_p \tag{1}$$

where the ω is a rotational velocity (rad/sec) and c, r and p represent the control frequency, rotor velocity and grid frequency; P is equal to 6 for the 4/8 machine. At low speed we want the control winding to be at 0 Hz up to about 50 Hz. This gives a speed range from 500 to 1000 rpm (Fig. 3 – solid line) which is a similar speed range to the equivalent DFIG machine (although slightly slower). At 750 rpm peak power is reached and the machine will then go into effectively a field weakening range, this corresponds to 25 Hz control winding frequency.

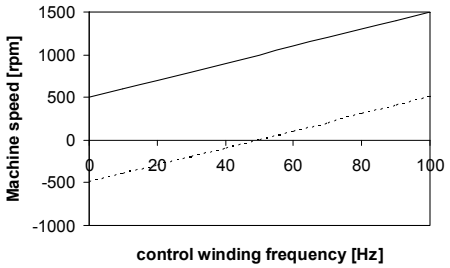

Fig. 3. Speed range for 4/8 machine (4-pole winding is control winding).

A. Basic sizing

If the target design is taken as 750 rpm for 2 MW then the torque is 26 kNm. From [11] the torque per rotor volume for an integral horse-power industrial motor could be up to 30 kNm/m^3.

This target speed is at maximum power but at this stage we are simply carrying out basic sizing, also since this is a larger machine then the torque per rotor volume should be high. Therefore the rotor will have volume of 26/30 = 0.86 m^3. Let us also assume a diameter to axial length ratio of a half then we can define the rotor diameter as 0.84 m and the axial length as 1.68 m. Sizing the stator is somewhat more complex, however, as an initial estimate the outer diameter is taken as double the rotor diameter at 1.68 m.

B. Winding arrangements

For such a large machine the number of slots would be high, possibly 72 slots or above. However, to maintain simplicity 48 slots are chosen here since it is the lowest possible number of slots for an 8 pole symmetrical winding. This arrangement is shown in Fig. 2. In Fig. 4 one phase of the 4 pole and one phase of the 8 pole windings are illustrated. The 8 pole winding has 32 turns-per-coil and the 4 pole winding has 32 turns-per-coil. If double layer windings were used then further refinement is possible with short pitching, particularly in the 4 pole winding.

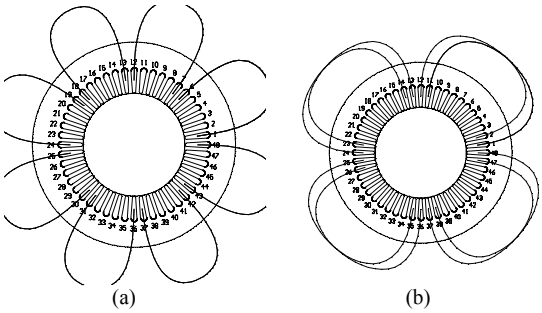

(a) (b)

Fig. 4. (a) 8-pole and (b) 4-pole phase windings.

C. *Open circuit simulations*

If the 8-pole power winding is excited with a phase current of 29.1 A rms (the current at maximum power at 1000 rpm) then a flux plot is shown in Fig. 5(a). In addition, a flux plot with the 4-pole winding excited only is also shown in Fig. 5 (b). This is carried out at 41.5 A to maintain the EMF in the power winding. While it is possible to observe flux patterns that may include 4 and 8 poles together, it is more correct to show the EMFs induced into the windings.

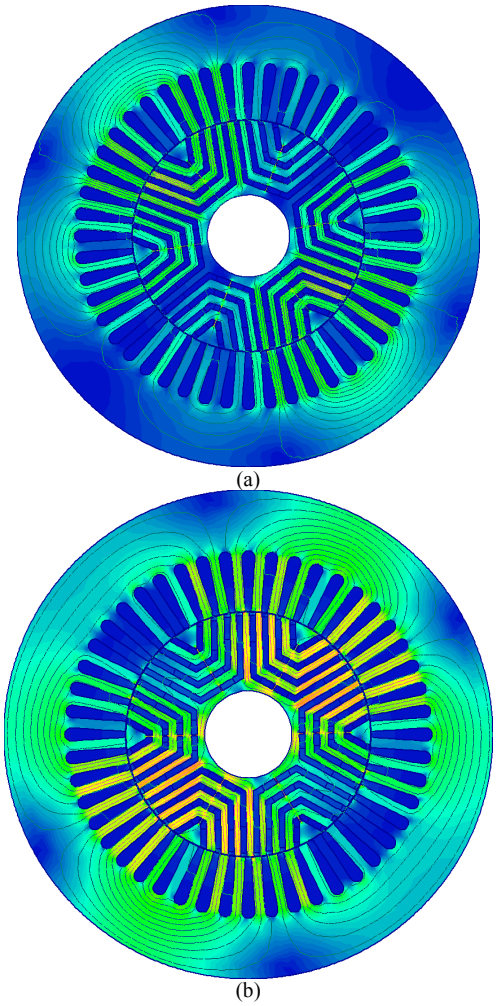

(a)

(b)

Fig. 5. Flux plots with (a) 8-pole winding exited only (29.5 A) and (b) 4-pole winding excited only (41.5 A).

With the geometry used in simulation and the winding described above the phase voltages when the 8-pole winding is excited are shown in Fig. 6 and for 4-pole excitation in Fig. 7. The current in the 4-pole winding in Fig. 7 is high and this produces some slotting effects as can be seen in the voltage waveform. However, this is a basic sizing exercise using current-fed static finite element solutions – more refinement of the rotor flux barrier to slot number ratio would help eliminate this. If the flux wave is investigated then the ripple is not as noticeable (as shown later under loaded conditions); the voltage is the differential of the flux linkage - an alternative would be to brake down the flux wave into its Fourier components and sum the differential terms. The higher ripple can be ignored.

It can be seen that voltages are suitable for up to 25 kV although the turns would be chosen to match the system (25kW is obviously high voltage requiring specialist winding – or reduced phase turns can be used to reduce the voltage then step up via a transformer). Bear in mind that the 8-pole winding is nominally the power winding, which is fixed in frequency and voltage whereas the 4-pole winding is the control winding with variable voltage and frequency. These waveforms appear reasonable for a first-pass design. In these simulations the rotor is notionally rotating at 1000 rpm so that the frequencies in both of the windings are 50 Hz. These results show that the FEA model of the machine produces reasonable results. The torque is assessed below using current-flux density loops as commonly used for torque prediction in reluctance and permanent magnet machines.

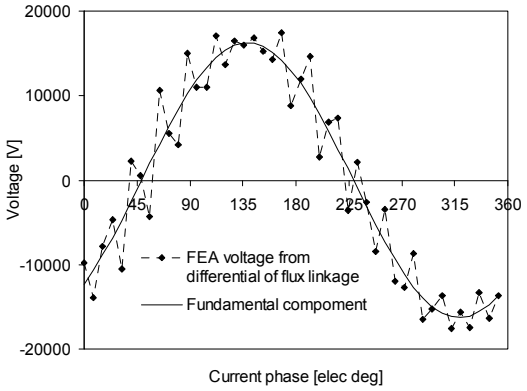

(a) power winding with current

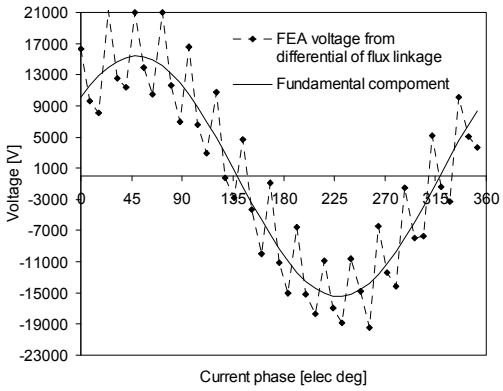

(b) control winding open circuit

Fig. 6. 8-pole excitation voltages (a) 8-pole winding with 29.5 A current – 11.5 kV rms, and (b) 4-pole open circuit voltages – 10.9 kV rms; 120 degree mechanical rotation at 1000 rpm.

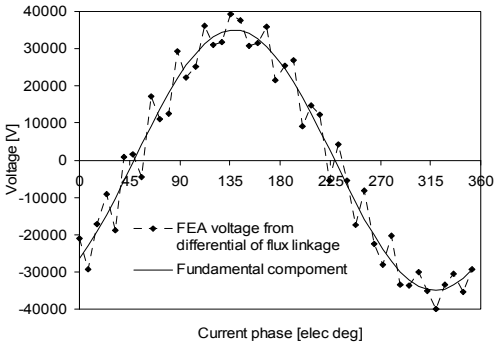

(a) control winding with current

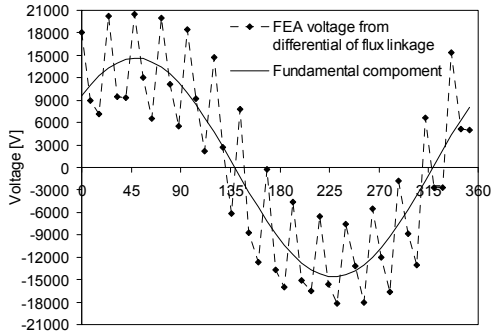

(b) power winding open circuit

Fig. 7. 4-pole excitation voltages (a) 4-pole winding with 41.5 A current – 24.7 kV rms, and (b) 8-pole open circuit voltages – 10.3 kV rms; 120 degree mechanical rotation at 1000 rpm.

III. SIMULATIONS

In this section we will examine the operation of the outlined machine topology using finite element analysis. Firstly we will address the basic equivalent circuit and obtain equations for the power delivered via each winding. This will illustrate why the 4 pole winding is used as the control winding and why the frequency of the control winding should be less that the power winding. The phasor diagram under load is obtained and then the torque and power are obtained from the finite element analysis using current – flux linkage loops (I-Psi loops).

A. Equivalent circuit and phasor diagram

The basic steady-state equivalent is given in Fig. 8. This can be used to predict the operation in the machine. From this circuit (note the use of generating convention for the current) the power generated is

$$\begin{aligned} P_{total} &= P_S + P_P = \mathrm{Re}\left\{\bar{E}_S \times \bar{I}_S^*\right\} + \mathrm{Re}\left\{\bar{E}_P \times \bar{I}_P^*\right\} \\ &= \mathrm{Re}\left\{j\omega_S M\ \bar{I}_P e^{-j\delta} \times \bar{I}_S^*\right\} + \mathrm{Re}\left\{j\omega_P M\ \bar{I}_S e^{-j\delta} \times \bar{I}_P^*\right\} \end{aligned} \quad (2)$$

If the current is maintained on the respective notional *q*-axes so that the current is in phase with the winding back-EMFs E_s and E_p then when the power and control windings have the same frequencies (i.e., at 1000 rpm) then the maximum power in each winding set is the same. However, as the speed reduces, say to 750 rpm, then the control winding frequency reduces to 25 Hz and now the control winding can only contribute half of the maximum power of the power winding because of the frequency terms in (2). The phasor diagrams are given in Fig. 9 for open-circuit operation (i.e., the power winding is not connected to the busbar) and full load operation at 1000 rpm. It can be seen that the control winding requires much more current on open-circuit because it has to induce the busbar voltage into the power winding. The phasor diagrams under load are at the point when the machine is under-excited and reactive power is being drawn from the supplies. To improve operation in terms of power factor, so that reactive power is generated rather than absorbed, then careful control needs to be implemented.

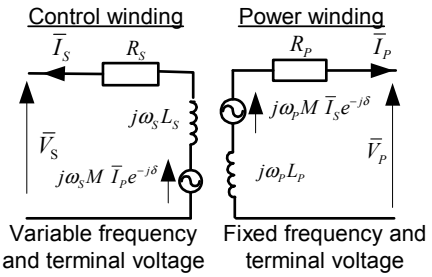

Fig. 8. Basic steady-state equivelant circuit.

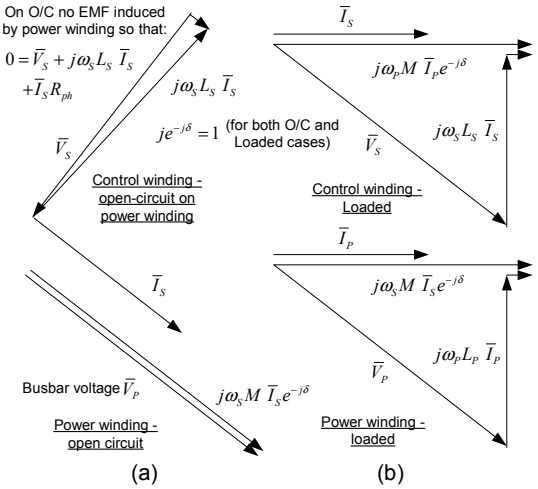

Fig. 9. Open-circuit on power winding and loaded phasor diagram – increased control winding current required on open-circuit to maintain busbar voltage on power winding.

B. Load simulations and I-Psi loops at 1000 rpm.

The machine was simulated at 1000 rpm with 59 A in the 4 pole control winding and 29.5 A in the power winding. The frequency in both windings is 50 Hz at this speed and equation (2) suggests that for maximum power at these currents then each winding contributes about the same power. In Fig. 10 the current – flux density (I-Psi) loops are shown for all three phases of each winding. The area enclosed in each loop represents the work done. The 4-pole winding contributes 0. 98 MW of electrical power and the 8 pole power winding contributes 0.97 MW. This gives a total of 1.95 MW which is close to the required (although this excluded copper losses, iron losses and friction and windage). There is some ripple in the flux linkage and when this is used to obtain the phase voltages that the characteristics as shown in Fig. 12 (power winding) and Fig. 13 (control winding) are obtained. As previously mentioned this arrangement is aimed at testing the possibility of realizing this machine at this size so that a more detailed design would use a different rotor/stator arrangement to reduce the voltage ripple.

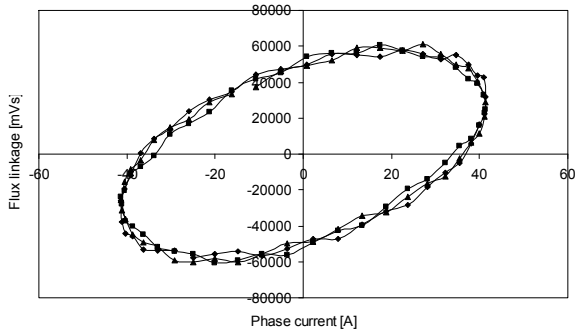

(a) 8-pole power winding

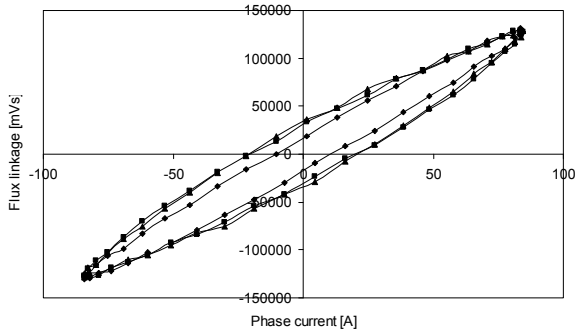

(a) 4-pole control winding

Fig. 11. I-Psi loops for machine with 29.5 A rms in control winding and 59 A rms in power winding at 1000 rpm.

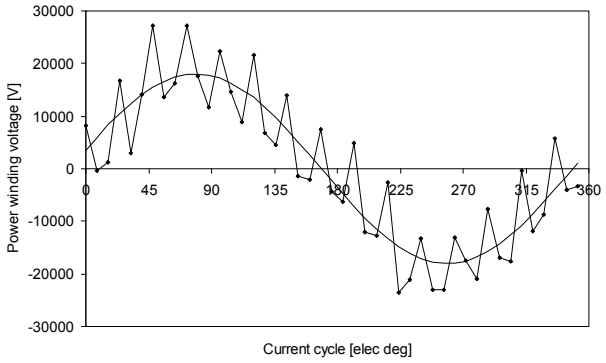

Fig. 12. Power winding phase voltage under load with 59 A rms in control winding and 29.5 A rms in power winding at 1000 rpm.

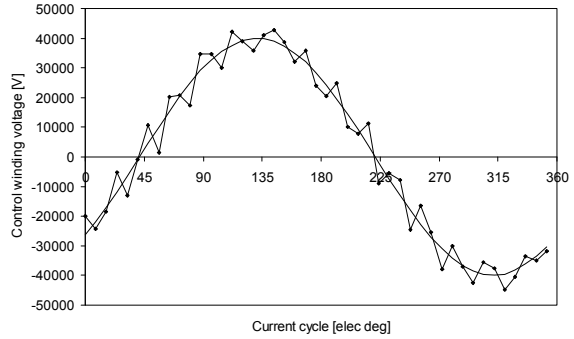

Fig. 13. Control winding phase voltage under load with 59 A in control winding and 29.5 A in power winding at 1000 rpm.

The power winding loop is an oval and the phase difference between the voltage and current is 30 deg. This gives a power factor of 0.87. However the loop of the control winding is relatively narrow with a voltage is 28.2 kV rms and the phase angle is 79 elec deg. This gives a power factor of 0.2. However, this point is when the currents are almost in phase with the induced back-EMFs so that the machine is operating very under-excited as illustrated in the phasor diagram in Fig. 9.

If the currents were made equal then the power factors can be improved. If we look at the open-circuit tests in Figs. 6 and 7 then we can calculate the X_P as 390 Ω ans $M_{S\text{-}P}$ to be 369 Ω from the voltages and excitation current (29.5 A rms) in power winding. However when the control winding is excited with 41.5 A then X_S is 595 Ω and $M_{P\text{-}S}$ is 249 Ω. In theory, the cross coupling should mean that $M_{P\text{-}S} = M_{S\text{-}P}$ but this is not the case. Inspection of the flux plots in Fig. 5 shows that when the control winding is excited with a higher current then there is considerably more flux in the machine and the rotor steel appears to be close to saturation. If the current is reduced to 29.5 A in the control winding when the power winding is open-circuit then X_S increases to 708 Ω and $M_{P\text{-}S}$ to 308 Ω. Hence this illustrates the point that this machine is operating close to its limit (as it should be due to the design approach).

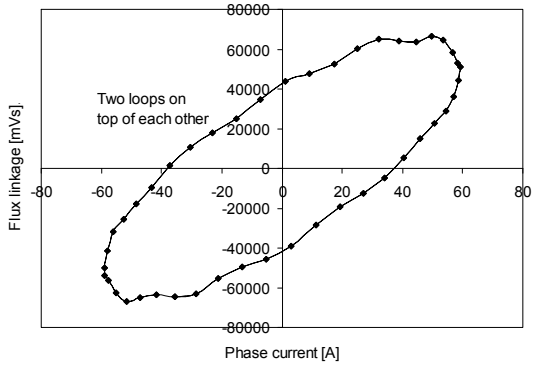

(a) 8-pole power winding (Phase 1 only)

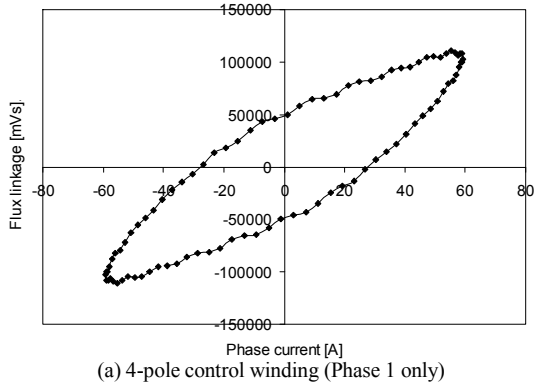

(a) 4-pole control winding (Phase 1 only)

Fig. 14. I-Psi loops for machine with 41.8 A rms in control winding and 41.8 A rms in power winding at 750 rpm.

C. Operation at 750 rpm

The speed in the simulation was reduced – this was done be carrying out a simulation over 180 mechanical degrees of movement. During this period the power winding will cycle through two complete current cycles and the control winding (now at 25 Hz) with cycle through one complete cycle. If the currents are set to 41.8 A in both windings and the speed reduced to 750 rpm the power from the 4 pole control winding was calculated to be 0.66 MW while the 8 pole power from the

power winding was 1.14 MW. This gives a total output power of 1.8 MW which is close the target 2 MW. The I-Psi diagrams are shown in Fig. 14. If can be seen that the areas of the loops are now larger and the voltage of the 8 pole winding is 15.6 V rms and the 4 pole winding is 16.1 V rms. The 4 pole power factor is now 0.58 and the 8 pole power factor is 0.33. These are still relatively low however the machine is still operating in under-excited mode.

D. Discussion

This section has given a basic arrangement for a possible 2 MW brushless doubly-fed reluctance machine. This is an exercise in scaling and illustrates the operation of the radially-laminated ducted rotor. This seems to give good results using a crude first-step design when simulated using 2D finite element analysis. There seems to be reasonable modulation by the rotor on the MMFs to get the required cross-coupling of the different pole-number windings. The machine was heavily loaded to check to see if there was any additional harmonic cross coupling. This was found to be a problem in the 2/6 machine in [1] and [2]. The cross-coupling is very important for correct operation. The voltage ripple can be traced to either numerical error or slotting effects and design and analysis refinement will alleviate this. The simulations used the I-Psi loops to obtain the torque and the flux linkage differential is used to obtain the voltage. The power factors appear to be low however the simulations kept the current close to the phase of E_P and E_C which is effectively under-excited operation.

IV. CONTROL

The model used in the finite element analysis represents a simple steady-state circuit for the machine to enable the basic sizing and testing of a 4 pole control winding and 8 pole power winding machine and this gave promising results for possible use in a 2 MW wind turbine generator. Here we will look at a detailed review of the control of this type of machine. It is tested on a 2/6 lab-based machine to validate the algorithm.

A. Dynamic Model

The space-vector equations in a stationary reference frame and the fundamental angular velocity relationship for the BDFRM torque production are [19]–[21]:

$$\mathbf{u}_p = R_p\mathbf{i}_p + \frac{d\boldsymbol{\lambda}_p}{dt} = R_p\mathbf{i}_p + \frac{d\boldsymbol{\lambda}_p}{dt}\Big|_{\theta_p=const} + j\omega_p\boldsymbol{\lambda}_p \tag{3}$$

$$\mathbf{u}_s = R_s\mathbf{i}_s + \frac{d\boldsymbol{\lambda}_s}{dt} = R_s\mathbf{i}_s + \frac{d\boldsymbol{\lambda}_s}{dt}\Big|_{\theta_s=const} + j(\omega_r-\omega_p)\boldsymbol{\lambda}_s \tag{4}$$

$$\boldsymbol{\lambda}_p = L_p\mathbf{i}_p + L_{ps}\mathbf{i}_s^* e^{j\theta_r} = \lambda_p e^{j\theta_p} \tag{5}$$

$$\boldsymbol{\lambda}_s = L_s\mathbf{i}_s + L_{ps}\mathbf{i}_p^* e^{j\theta_r} = \lambda_s e^{j\theta_s} \tag{6}$$

$$\omega_r = d\theta_r/dt = p_r\omega_{rm} = \omega_p + \omega_s \tag{7}$$

where $L_{p,s,ps}$ represent the 3-phase inductances of the grid-connected (primary or power) and inverter-fed (secondary or control) windings [21][22], ω_{rm} is the rotor angular velocity (rad/s) at which the machine develops useful torque, p_r is the number of rotor poles, $\omega_{p,s}$ are the applied frequencies to the windings. Note that $\omega_s > 0$ for super-synchronous operation and $\omega_s < 0$ if the machine is operated below the synchronous speed. At synchronous speed $\omega_s = 0$, i.e., the secondary side is DC supplied as with a classical $2p_r$-pole synchronous machine. The 'negative' secondary frequency in the sub-synchronous mode simply means the opposite phase sequence of the secondary to the primary winding. The angular positions of various phasors in (3) to (6) are defined in Fig. 7.

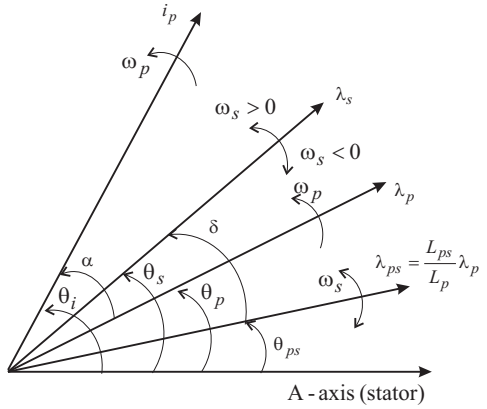

Fig. 15. Characteristic phasors in a stationary reference frame.

B. Sensorless reactive power control

A detailed description and performance evaluation of the DTC scheme for the BDFRM developed was put forward in [15], [16] and [17]. One of the BDFRM's main attributes is its power factor control capability [24]. The power factor in the secondary winding is directly related to the inverter size, but is irrelevant to the outside utility network (since the inverter effectively isolates the secondary from the mains supply). However the power factor of the primary winding is of great importance to the utility grid (especially in weak networks) in the light of reactive power requirements. To minimize the total current loading (and thus losses) for a given real power demand, it is therefore desirable to keep the primary power factor at or, as close as possible to unity.

Using the primary flux oriented forms of (3)-(6) the secondary flux expression for optimization of the primary power factor or any other performance indicator of the machine can be derived. It was shown in [23] and [24] that the maximum primary power factor (MPPF), i.e., no reactive power flow through the primary winding:

$$Q_p = \frac{3}{2}\frac{\omega_p\lambda_p}{L_p}\left(\lambda_p - L_{ps}\cdot i_{sd}\right) = 0$$

is achieved if $i_{sd} = \lambda_p / L_{ps}$. Under this condition, the MPPF secondary flux reference for a desired torque (Fig. 15) and this can be expressed as:

$$\lambda_s^* = \sqrt{\underbrace{\left(\frac{L_s}{L_{ps}}\cdot\lambda_p\right)^2}_{\lambda_{sd}} + \underbrace{\left(\frac{\sigma L_{ps}}{1-\sigma}\cdot\frac{2T_e^*}{3p_r\lambda_p}\right)^2}_{\lambda_{sq}}} \tag{8}$$

where $\sigma = 1 - L_{ps}^2/(L_pL_s)$ is the leakage factor and i_{sd} is the d-axis secondary current aligned with the mutual flux vector, i.e., λ_{ps} in Fig. 15. It can be seen from (8) that $\lambda_{sd} \approx const$ irrespective of the machine loading due to the primary winding

grid connection, i.e., $\lambda_p \approx const$. This fact is important as it means that the torque producing λ_{sq} component can be controlled indirectly via λ_s but in a stationary (and not rotating) frame. In other words, the DTC can be optimized since in this case vector control problem is reduced to a single variable effectively becoming scalar in nature. For the scope of this paper, a significant benefit of greater control freedom, afforded by the accessibility of both BDFRM windings, is the possibility of sensorless speed control [17]. The rotor angle can be retrieved from (5):

$$\theta_r = \tan^{-1} \frac{\mathrm{Im}\left[\left(\boldsymbol{\lambda}_p - L_p \cdot \mathbf{i}_p\right) \cdot \mathbf{i}_s\right]}{\mathrm{Re}\left[\left(\boldsymbol{\lambda}_p - L_p \cdot \mathbf{i}_p\right) \cdot \mathbf{i}_s\right]} \tag{9}$$

The raw position estimates are then input into a Luenberger type PI observer [18] to predict the rotor angular velocity $\omega_r = \mathrm{d}\theta/\mathrm{d}t$ used for the speed control as shown in Fig. 1. Excellent low pass filtering abilities of this observer, anticipated by simulations in [18], have been experimentally verified by results which are presented below. It should be mentioned here that the rotor position information is only required for speed estimation and not for torque control, since the method is stator-frame-based, as is usual for DTC.

C. Experimental Results

The sensorless algorithm in Fig. 2 has been implemented and executed in dSPACE for the MPPF control strategy on a scaled-down 6/2-pole BDFRM prototype. Details of the test system and the relevant machine parameters can be found in [15] and [16].

The top plots in Fig. 16 represent the rotor angles obtained from (9), and their absolute variations from encoder measurements. The raw estimates are noisy, but despite the error spikes, which have been found to be largely due to the practical effects such as measurement noise and sensitivity to parameter knowledge inaccuracies, the average estimation error is still reasonably low (≈ 7º). The effectiveness of the observer as a low-pass filter is evident from the same figure (bottom plots), and a significant improvement in accuracy is achieved by processing θ_r through it. The average error is reduced to approximately 1.5º with the maximum values being about 3.4º or less. The main reason for such a high accuracy is the quality estimates being fed into the observer by the position estimator which, similarly to the latter, works in a closed-loop fashion as illustrated in Fig. 2.

Fig. 17 shows the speed waveform for changes in desired speed values between 950 rpm, 750 rpm and 550 rpm. In this case, the speed limits correspond to f_s = 13.3 Hz in either mode. It can be seen that the machine may be effectively controlled over the considered speed range, including synchronous speed (750 rpm) when f_s = 0. Reliable low-frequency operation of the BDFRM is an important point of the proposed sensorless scheme, and certainly represents a significant advantage over traditional DTC and many other back-EMF based control methods. These have difficulties (or simply do not work) in this frequency region even in sensor speed mode. It should be emphasized that the gains of both the speed PI regulator and the observer must be lowered and appropriately tuned as instability and divergence of the control algorithm may otherwise occur due to the noisy input estimates. This trade-off results in low bandwidth control and relatively modest dynamic response of the machine which is, fortunately, quite acceptable for the target applications where steady-state performance is of more interest.

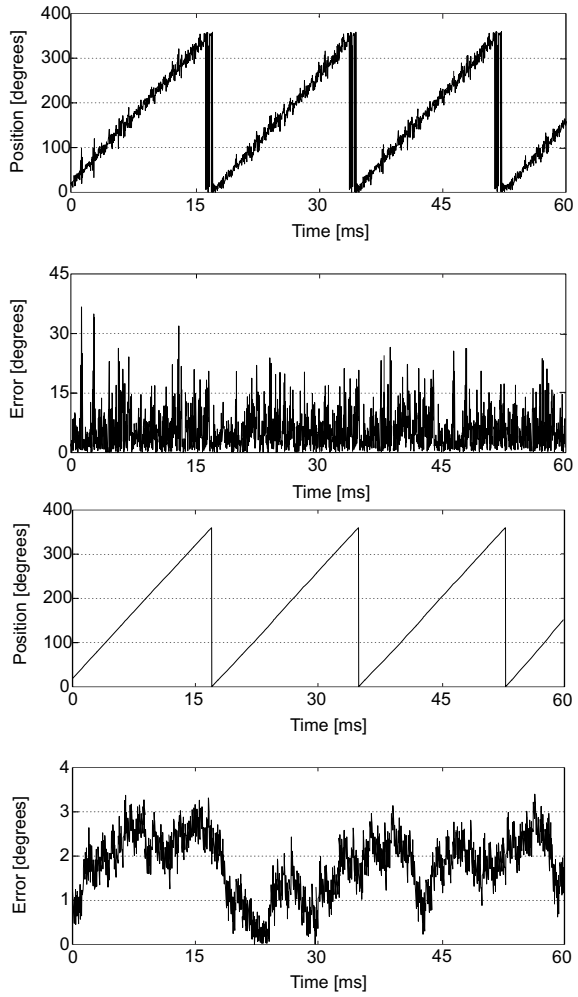

Fig. 16. Estimated (top) and observed (bottom) rotor position at 850 rpm (f_s = 6.7 Hz).

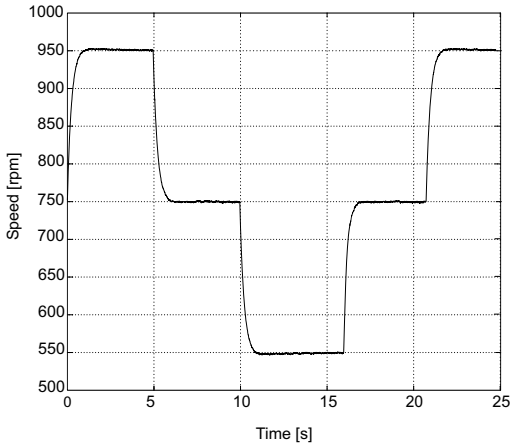

Fig. 17. Sensorless control performance down to synchronous speed.

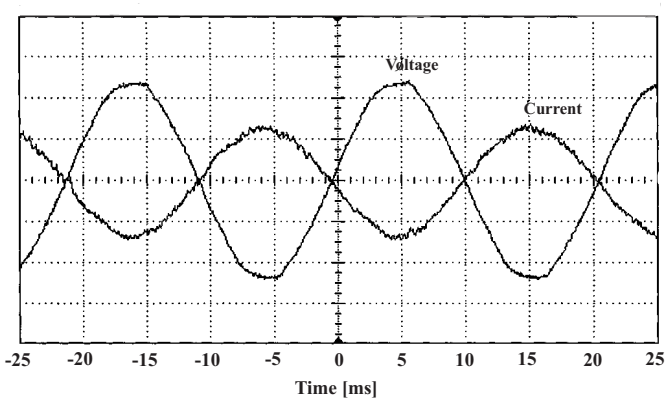

Fig. 18. Primary voltage and current waveform for unity power factor.

The oscilloscope traces for primary winding voltage and current in Fig. 18 clearly demonstrate that the intended maximum primary factor operation has been successfully achieved. Note that the respective waveforms are smooth, virtually switching ripple-free (due to the relatively weak magnetic coupling between the windings being inherent with this particular machine) and at line frequency (50 Hz). Similar results could be obtained for unity (or even leading) line power factor control in which case the secondary side would be entirely responsible for the machine magnetization by providing the necessary reactive power to the primary (or to the grid) at the expense of increased inverter loading.

CONCLUSIONS

This paper puts forward a description of a realistic design for a brushless doubly-fed machine that is of practical value. It takes the form a 4-pole - 8-pole machine aimed for use in a 2 MW wind turbine over a correct speed and torque range. Previous examples discussed laboratory machines and this study takes the outcomes from these studies to formulate a procedure for sizing and designing the machine. A radially-laminated ducted rotor design is studied and this produces good modulation and cross-coupling between the two different pole-number windings. Finite element analysis is used in conjunction with I-Psi loops to validate the basic design. Control is also addressed in the second part of the paper. The work illustrates that power factor control is necessary and this is a major issue with this machine. Sensorless control is assessed as a possible control strategy. This paper is aimed at taking the machine from a small-scale laboratory example to consideration as a large-size industrial generation.

REFERENCES

[1] I. Scian, D. G. Dorrell, and P. Holik, "Assessment of Losses in a Brushless Doubly-Fed Reluctance Machine", IEEE Transactions on Magnetics, INTERMAG special edition, October 2006.

[2] D. G. Dorrell, I. Scian, E. M. Schulz, R. B. Betz and M. Jovanovic, "Electromagnetic Considerations in the Design of Doubly-Fed Reluctance Generators for use in Wind Turbines" IEEE Industrial Electronics Conference, IECON, Paris 7-10 Nov. 2006.

[3] R. E. Betz and M. G. Jovanovic, "The Brushless Doubly Fed Reluctance Machine and the Synchronous Reluctance Machine - A Comparison", IEEE Trans on Industry Applications, Vol. 36, No. 4, July/August 2000.

[4] R. B. Betz and M. G. Jovanovic, "Theoretical Analysis of Control Properties for the Brushless Doubly Fed Reluctance Machine", IEEE Trans on Energy Conversion, Vol 17, No 3, Sept 2002, pp 332-339.

[5] M. G. Jovanovic and R. E. Betz, "The Use of Doubly Fed Reluctance Machines for Large Pumps and Wind Turbines", IEEE Trans on Industry. Applications, Vol 38 No 6, Nov 2002, pp 1508-1516.

[6] M. G. Jovanovic and J. Yu, "An Optimal Direct Torque Control Strategy for Brushless Doubly-Fed Reluctance Motors", IEEE Power Electronics and Drive Systems Conference, 17-20 Nov 2003, Vol 2, pp 1229-1234.

[7] M. G. Jovanovic, "Control of Brushless Doubly-Fed Reluctance Motors", IEEE International. Symposium. on Industrial Electronics, 2005, Dubrovnik, Croatia, pp 1667-1672.

[8] E. M. Shulz, and R. E. Betz, "Optimal Torque per Amp for Brushless Doubly Fed Reluctance Machines", 40th IEEE IAS Meeting, 2-6 Oct, 2005, Hong Kong, pp 1749-1753.

[9] D. G. Dorrell, I. Scian, and P. J. Holik, "Assessment of the Electromagnetic Performance of Doubly-Fed Reluctance Machines for Use in Variable Speed Generators", ICEMS, Nagasaki, Japan, 20-23 Nov 2006.

[10] D. G. Dorrell, "Design Requirements for Doubly-Fed Reluctance Generators", IEEE PEDS Conference, Bangkok, Thailand, Dec 2007.

[11] J. R. Hendershot and TJE Miller, "Design of Brushless Permanent Magnet Motors", Oxford Science Publications, 1994.

[12] P.Bauer, S. de Haan, C.R.Meyl, and J.T.G.Pierik, "Evaluation of electrical systems for off-shore windfarms," IAS Annual Meeting, Rome, Italy, 2000.

[13] F.Wang, F.Zhang, and L.Xu, "Parameter and performance comparison of doubly-fed brushless machine with cage and reluctance rotors," IEEE Transactions on Industry Applications, vol. 38, pp. 1237–1243, Sept/Oct 2002.

[14] Y. Liao and C. Sun, "A novel position sensorless control scheme for doubly fed reluctance motor drives," IEEE Transactions on Industry Applications, vol. 30, pp. 1210–1218, Sept/Oct 1994.

[15] M.G.Jovanovic, J.Yu, and E.Levi, "Direct torque control of brushless doubly fed reluctance machines," Electric Power Components and Systems, vol. 32, pp. 941–958, October 2004.

[16] M.G.Jovanovic, J.Yu, and E.Levi, "Encoderless direct torque controller for limited speed range applications of brushless doubly fed reluctance motors," IEEE Transactions on Industry Applications, vol. 42, pp. 712–722, May/June 2006.

[17] M.G.Jovanovic, J.Yu, and E.Levi, "A doubly-fed reluctance motor drive with sensorless direct torque control," IEEE International Electric Machines and Drives Conference (IEMDC), Madison, Wisconsin, June 2003.

[18] R. Lorenz and K. Patten, "High-resolution velocity estimation for all-digital, ac servo drives," IEEE Trans. on Industry Applications, vol. IA-27, pp. 701–705, July/August 1991.

[19] F. Liang, L. Xu, and T. Lipo, "D-q analysis of a variable speed doubly AC excited reluctance motor," Electric Machines and Power Systems, vol. 19, pp. 125–138, March 1991.

[20] Y. Liao, L. Xu, and L. Zhen, "Design of a doubly-fed reluctance motor for adjustable speed drives," IEEE Transactions on Industry Applications, vol. 32, pp. 1195–1203, Sept/Oct 1996.

[21] R.E.Betz and M.G.Jovanovic, "Introduction to the space vector modelling of the brushless doubly-fed reluctance machine," Electric Power Components and Systems, vol. 31, pp. 729–755, August 2003.

[22] R.E.Betz and M.G.Jovanovic, "The brushless doubly fed reluctance machine and the synchronous reluctance machine - a comparison," IEEE Transactions on Industry Applications, vol. 36, pp. 1103–1110, July/August 2000.

[23] L. Xu, L. Zhen, and E. Kim, "Field-orientation control of a doubly excited brushless reluctance machine," IEEE Transactions on Industry Applications, vol. 34, pp. 148–155, Jan/Feb 1998.

[24] M. G. Jovanovic and R. E. Betz, "Power factor control using brushless doubly fed reluctance machines," Proc. of the IEEE-IAS Annual Meeting, Rome, Italy, October 2000.